



Radial throw in micromachining: Measurement and analysis[☆]

Sudhanshu Nahata^a, Recep Onler^a, Shivang Shekhar^a, Emrullah Korkmaz^a,
O. Burak Ozdoganlar^{a,b,c,*}

^a Department of Mechanical Engineering, Carnegie Mellon University, Pittsburgh, PA 15213, USA

^b Department of Materials Science and Engineering, Carnegie Mellon University, Pittsburgh, PA 15213, USA

^c Department of Biomedical Engineering, Carnegie Mellon University, Pittsburgh, PA 15213, USA

ARTICLE INFO

Keywords:

Micromachining
Run-out
Radial throw
Spindle metrology
Ultra-high-speed spindles
Micromilling

ABSTRACT

This paper presents a comprehensive approach for measurement and analysis of radial throw and the associated tool-tip trajectory in micromachining when using ultra-high-speed (UHS) spindles. The effect of radial throw on micromachining accuracy could be significant due to the strict absolute-tolerance requirements. However, accurately determining radial throw in micromachining poses challenges due to the micron-scale tool dimensions and high rotational speeds. In contrast to *run-out*, radial throw depends on the tool-rotation angle and dictates the instantaneous position (trajectory) of the cutting edges. This work first presents a mathematical framework to obtain the radial throw at the cutting edges by measuring radial throw at two locations on the tool shank. A laser Doppler vibrometry-based experimental approach is then described to accurately measure the radial throw from the tool shank in two mutually-perpendicular directions. Next, the variations on radial throw measurements are evaluated, the effect of spindle speed on the radial throw is analyzed, and the predictions of tool-tip radial throw are compared with those directly measured from the tip of a micro-tool blank. A study is then performed to assess the effect of tool attachment/detachment cycles on radial throw. Lastly, a set of simulations is conducted to demonstrate how the radial throw magnitude and orientation affect the surface location error, sidewall surface roughness, and flute-to-flute chip-thickness variations. It is concluded that the presented mathematical framework and measurement approach can be used to determine the tool-tip radial throw magnitude with better than $3.5\% \pm 2\%$ accuracy. Increased spindle speed considerably increases the radial throw, e.g., from $8\ \mu\text{m}$ at 60,000 rpm to $16\ \mu\text{m}$ at 130,000 rpm. The tool attachment/detachment induces less than $\pm 6.9\%$ variation to the mean radial throw magnitude at 60,000 rpm. The main contributor to the variation of the radial throw orientation is identified as the inherent inaccuracies of the spindle.

1. Introduction

Micromachining processes, such as micromilling, are used by many industries for fabricating three-dimensional (3D) micro-scale parts with complex geometries [1–4]. Absolute tolerance requirements for micromachining processes are very strict due to the micron-scale dimensions of the fabricated features. One of the major contributors to the dimensional/form errors and surface roughness of the micromachined features is the radial throw of the tool axis. Radial throw causes the trajectory of each cutting point to deviate from the ideal trajectory, which is a circle with a diameter equal to the tool diameter. As explained in international standards [5], in contrast to *run-out*, which indicates the total displacement of a rotating surface within a full rotation at a given axial location, *radial throw of a rotary axis* describes the instantaneous position of a geometric axis at a given axial location, and

thus, depends on the rotation angle [5]. In micromachining, the magnitude of radial throw can be commensurate with the prescribed feed value, thereby altering the instantaneous chip thickness significantly [6]. Therefore, radial throw is critical not only for dimensional, form, and surface accuracy, but also for the micromachining forces and process-modeling efforts. However, accurately determining radial throw in micromachining is challenging due to the micron-scale tool dimensions and high rotational speeds.

Radial throw arises from the geometric inaccuracies of the tool-collet-spindle assembly and from the interfaces between the components of the assembly. When measured at low rotational speeds, the radial throw only reflects the geometric inaccuracies of the assembly. Rotational motion further increases the magnitude of radial throw due to the rotating unbalance effect. This effect is controlled by the dynamic response of the assembly to the forces resulting from the misalignment

[☆] This paper was recommended by Associate Editor Christopher Tyler.

* Corresponding author at: Department of Mechanical Engineering, Carnegie Mellon University, Pittsburgh, PA 15213, USA.
E-mail address: ozdoganlar@cmu.edu (O.B. Ozdoganlar).

(unbalance) between the rotational and the geometric axes [5]. The magnitude and form of this *dynamic component of radial throw* depend on both the amount of misalignment and the dynamics of the assembly. For example, as the spindle speed approaches a resonant frequency of the assembly, radial throw increases significantly and its form changes [7]. Furthermore, the dynamic behavior of the assembly may not be axisymmetric at every frequency (i.e., it is not identical in two mutually-perpendicular directions). Such lack of axisymmetry could cause the rotational axis to follow an elliptical, rather than a circular, trajectory [7–9]. Therefore, radial throw must be measured at different spindle speeds along two mutually-perpendicular directions simultaneously. Furthermore, the contributions to radial throw from the tool-collet-spindle assembly and the dynamic response should be analyzed.

In micromachining, important contributors to radial throw include the tool-collet-spindle assembly and the associated interfaces, the dynamic behavior of the assembly, and the spindle-error motions [7,10,11]. In particular, the largest contribution commonly occurs at the rotational frequency as one-per-revolution (one-per-rev) motions, since the spindle error motions (synchronous and asynchronous) are commonly much smaller than one-per-rev components for UHS spindles [10,11]. The tool-geometry errors could also contribute significantly to radial throw [12]. In this work, we focus on the one-per-rev component of the radial throw arising from the assembly and its interfaces, spindle-error motions, and the dynamic response to rotating unbalance forces. Although the tool-geometry errors are not considered here (and will be considered in our future work), the framework presented here allows inclusion of those errors if they are known.

Accurate determination of radial throw from micro-tools when using UHS spindles poses various challenges. First, due to the fragile nature of the micro-tools and the need for measuring radial throw from the rotating surfaces at high rotational speeds, a non-contact measurement technique is needed. Second, being able to measure at high rotational speeds also necessitates the use of high frequency-bandwidth instruments. Third, considering relatively small radial throw magnitudes and the sensitivity of the tilt angle calculations to the resolution of the measurements, high precision measurement instrumentation is required (e.g., accuracy better than 10 nm, and resolution better than 1 nm). And fourth, since the form of the radial throw could be non-circular, measurements should be conducted simultaneously from two mutually-perpendicular directions. In combination, these requirements eliminate simple measurement approaches (e.g., by using dial gages or optical microscopes). Laser Doppler vibrometry (LDV) [13,14] and capacitance probe-based techniques [15] are the two leading candidates that satisfy all the aforementioned needs, although the latter has limitations in both frequency bandwidth (< 15 kHz) and its capability for measuring from surfaces with high curvature (e.g., small diameter cylinders) [16]. In any case, direct measurements from the micro-scale fluted region while satisfying these requirements are not possible since the cutting flutes cause the displacement signal to drop due to sharp changes in surface location and normal. As such, determination of the radial throw at the tool-tip entails making multiple measurements from the shank region of the micro-tools and calculating the radial throw using a mathematical approach. The orientation of the cutting edges with respect to the instantaneous radial throw must be known to determine the trajectory of each cutting point.

There has been a number of efforts in the literature to obtain the radial throw or run-out at the tool-tip when using UHS spindles. A few studies proposed analyzing the process outputs, such as cutting forces [17–19] or feed marks [20], to predict the run-out at the tool-tip. However, those indirect methods have yielded inaccurate results, mainly due to a lack of means to precisely measure process outputs and isolate the run-out from inherent process variabilities, such as those from the workpiece material. Other researchers performed high-accuracy displacement measurements to obtain the radial motions of rotating artifacts or micro-tools at varying spindle speeds. Liu et al. [21] used a capacitive-probe based method to measure run-out and the

orientation of the maximum radial throw (which was referred to as run-out) from a single point on the tool shank at varying spindle speeds. Similarly, Anandan et al. [11] conducted the radial measurements from a single point on the surface of a precision artifact using an LDV-based technique. They analyzed speed-dependent fundamental (one-per-rev) and spindle-error (synchronous and asynchronous) motions using these measurements. Although their work captured the effect of spindle speed on radial throw of the rotational axis, the trajectory of each cutting point cannot be calculated from their measurements since the tilt and cutting-edge orientations (with respect to the measured radial motions) were not obtained. Jun et al. [12] performed single-axis measurements of run-out at multiple points on the surface of a micro-tool shank using a capacitance probe. From those measurements, they predicted the run-out and its orientation at the micro-tool tip to calculate the instantaneous chip loads. They considered the contributions of the eccentricity and tilt in tool-attachment, as well as the tool-geometry errors. More recently, Anandan et al. [22] used an LDV based technique and conducted measurements at two different axial planes from the surface of a cylindrical gage pin to obtain the tilt information in addition to the radial motions. Although the aforementioned studies provide a foundation for measuring radial motions from micro-tool surfaces, a comprehensive, experimentally validated approach to determine the radial throw at each cutting point and the associated analysis to reveal the effects of spindle speed, dynamics, and statistical variation of radial-throw parameters have yet to be completed.

This paper presents an approach for the accurate determination of the spindle speed-dependent radial throw at the tool-tip and the associated trajectory of cutting points for microtools rotated on a UHS micromachining spindle. First, a mathematical framework to enable determining radial throw and the associated trajectory of cutting points is presented. The framework uses measurements of radial throw from two mutually perpendicular axis at two locations along the micro-tool shank. Next, the experimental setup and techniques for LDV-based measurements of radial throw are described. The proposed approach is then validated by comparing the predicted radial throw at the tip of a micro-tool blank to that measured directly from the tip. To assess the statistical distributions of radial throw parameters arising from tool attachment-detachment cycles, a number of radial throw measurements are conducted and analyzed. Next, simulations are performed to examine the effects of radial throw magnitude, orientation and form on dimensional accuracy (channel width), surface roughness (on channel sidewalls) and chip-load variations. This work builds upon the authors' previous work in [11] and expands it to provide a comprehensive approach for measurement and analysis of radial throw, including a general mathematical framework for determination of radial throw at any cutting point; a direct validation of the radial throw predictions; an assessment of variations and associated sources in radial throw measurements; a statistical analysis of tool-attachment errors; and an evaluation of the effects of spindle, collet, and the tool on radial throw orientation.

2. A mathematical framework to determine the radial throw

In this section, we provide the nomenclature and present the mathematical framework that will be used to determine radial throw at the tool-tip and the associated trajectory of each cutting edge. Fig. 1 illustrates the end of a micro tool as it rotates on a spindle. The tool rotates about an axis z , which is referred to as the rotational axis or the axis average line. Two mutually-orthogonal axes, x and y , defined perpendicular to the z axis, form the plane illustrated in Fig. 1. The radial throw of the (tool) axis is defined by the vector $\rho(z, \theta)$. Here, θ indicates the angle of rotation of the tool measured counter-clockwise (ccw) from the x axis to the “first” cutting edge C_1 at the tool-end plane; and z is the axial location of the measurement plane, where $z = 0$ is at the spindle nose. The trajectory of the m^{th} cutting edge, p_m , on the z plane can be written as

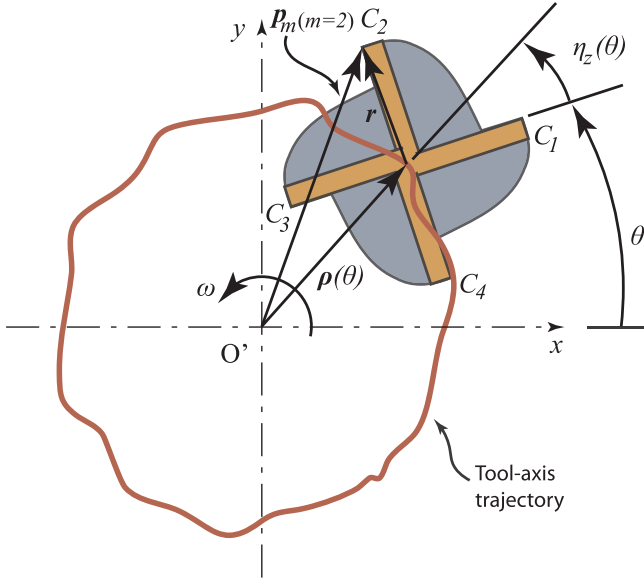


Fig. 1. Description of radial throw, $\rho(\theta)$. The magnitude of radial throw is significantly exaggerated in this figure to help the visualization. C_m indicates the m^{th} cutting edge.

$$\mathbf{p}_m(z, \theta) = (\rho_x(z, \theta) + r \cos(\theta + 2\pi(m-1)/n))\mathbf{i} + (\rho_y(z, \theta) + r \sin(\theta + 2\pi(m-1)/n))\mathbf{j}, \quad (1)$$

where \mathbf{i} and \mathbf{j} are the unit vectors along the x and y directions, respectively. Here, ρ_x and ρ_y are the x and y components of ρ , r is the radius of the cutting tool, and n is the number of cutting flutes. The orientation of the radial throw, $\eta_z = \eta_z(\theta)$, is defined as the angle measured ccw from the reference (first) cutting edge to the radial throw vector at a given axial location z .

Fig. 2(a) describes the tool axis and its relation to the rotational axis z . The tool axis, which is assumed to be straight, is defined with a vector \mathbf{q} that extends out of the spindle nose (from point A). The eccentricity vector, \mathbf{e} , is the radial throw of the (tool) axis at the $z = 0$ plane (see Fig. 2(b)). As seen in Fig. 2(b) and (c), the radial throw orientation (η_z) changes with z . The effect of tilt at any axial location z can be represented by a vector \mathbf{EB} , obtained by projecting \mathbf{q} on the x - y plane. The orientation of the vector \mathbf{EB} is defined by the angle $\delta = \delta(\theta)$ measured ccw from $\mathbf{O_zE}$, which is the projection of the eccentricity vector on the same plane.

Determination of the trajectory \mathbf{p}_m at each cutting point entails calculation of each of the parameters in Eq. (1). This is done by measuring the radial throw at two axial positions (z_1 and z_2) of the tool

shank along the x and y directions. Those measurements provide x and y components of ρ at the two axial locations, i.e.,

$$\begin{aligned} \rho_1 &= \rho(z_1, \theta) = \rho_{1x}\mathbf{i} + \rho_{1y}\mathbf{j}, \quad \text{and} \\ \rho_2 &= \rho(z_2, \theta) = \rho_{2x}\mathbf{i} + \rho_{2y}\mathbf{j}. \end{aligned} \quad (2)$$

From Fig. 2(a), we can write a vector equation

$$\rho_1 + \mathbf{q}_{12} = (z_2 - z_1)\mathbf{k} + \rho_2, \quad (3)$$

where $\mathbf{q}_{12} = \mathbf{q}_{12}(\theta)$ indicates the vector along the tool axis spanning from the z_1 plane to the z_2 plane, and \mathbf{k} is the unit vector along the z direction. Since ρ_1 , ρ_2 and $(z_2 - z_1)$ are known from the measurements, using Eq. (3), the unit vector $\mathbf{e}_q = \mathbf{e}_q(\theta)$ along the tool axis \mathbf{q} can be calculated as

$$\mathbf{e}_q = \frac{\mathbf{q}_{12}}{|\mathbf{q}_{12}|} = \frac{\rho_2 - \rho_1 + (z_2 - z_1)\mathbf{k}}{|\rho_2 - \rho_1 + (z_2 - z_1)\mathbf{k}|}. \quad (4)$$

Furthermore, the tilt angle, which is the acute angle between the rotational axis z and the tool axis, can be determined from

$$\zeta(\theta) = \cos^{-1}(\mathbf{e}_q \cdot \mathbf{k}), \quad (5)$$

where “ \cdot ” indicates the inner product operation.

At this point, finding the eccentricity vector \mathbf{e} from the measurements will simplify the determination of the radial throw at any cutting point along the flutes. To determine the eccentricity vector, we again consider Fig. 2(a) and write the vector equation

$$\mathbf{e} + \mathbf{q}_{01} = z_1\mathbf{k} + \rho_1, \quad \text{yielding } \mathbf{e} = z_1\mathbf{k} + \rho_1 - \mathbf{q}_{01}. \quad (6)$$

Here, \mathbf{q}_{01} is the vector along the tool axis spanning from the spindle nose ($z = 0$ plane) to the z_1 plane, and can be calculated as

$$\mathbf{q}_{01} = \frac{z_1}{\cos(\zeta(\theta))}\mathbf{e}_q \quad (7)$$

The radial throw of the axis at any axial location z satisfies the vector equation (refer to Fig. 2(a))

$$\rho(z, \theta) + z\mathbf{k} = \mathbf{q}_{0z} + \mathbf{e} \quad (8)$$

where $\mathbf{q}_{0z} = (z/\cos\zeta(\theta))\mathbf{e}_q$. Thus, $\rho(z, \theta)$ can now be written as

$$\rho(z, \theta) = \frac{z}{\cos\zeta(\theta)}\mathbf{e}_q + \mathbf{e} - z\mathbf{k}. \quad (9)$$

Therefore, trajectory of a cutting point can now be determined by finding $\rho_x(z, \theta) = \rho(z, \theta) \cdot \mathbf{i}$ and $\rho_y(z, \theta) = \rho(z, \theta) \cdot \mathbf{j}$ from Eq. (9) and substituting them into Eq. (1). The orientation of $\rho(z, \theta)$ can now be given as

$$\eta_z = \cos^{-1}\left(\frac{\rho(z, \theta) \cdot \mathbf{i}}{|\rho(z, \theta)|}\right) - \theta. \quad (10)$$

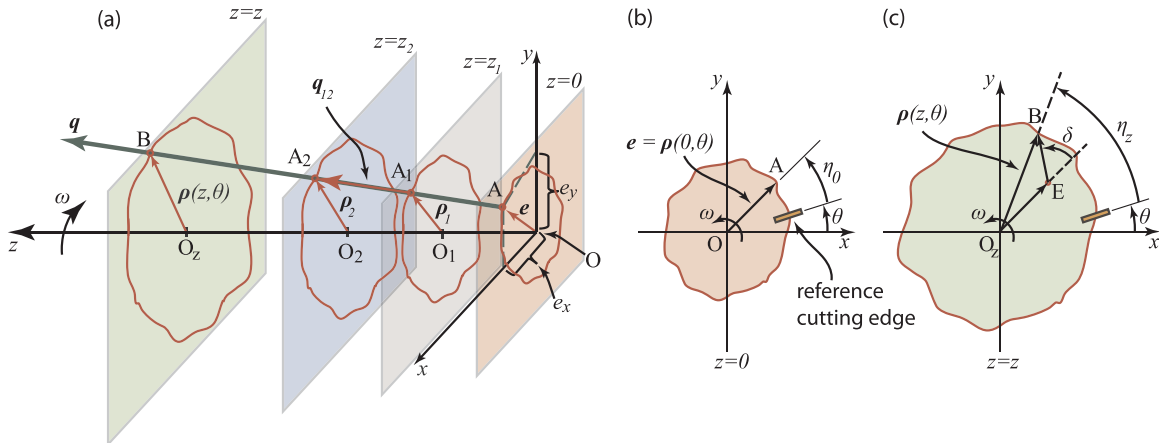


Fig. 2. (a) Radial throw and its relation to the rotational axis, (b and c) parameters of radial throw for two x - y planes located at $z = 0$ and $z = z$, respectively.

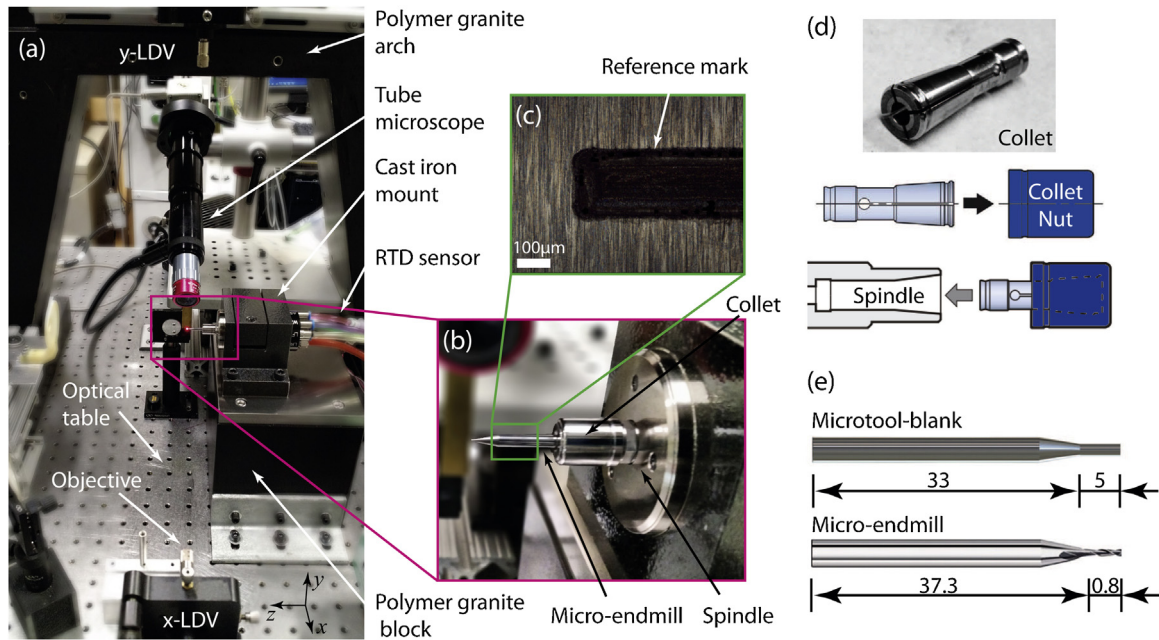


Fig. 3. (a) The experimental setup used for the measurement of radial throw, (b) a micro-endmill attached to the spindle, (c) the reference mark on the tool, (d) a four-jaw collet and clamping of collet using a collet nut, and (e) the microtool-blank and the micro-end mill used in this work (dimensions not to scale.)

3. Experimental methods

3.1. Experimental setup

The experimental setup used in this work is shown in Fig. 3. The radial motions are measured using two laser Doppler vibrometers (LDVs) with fiber-optic laser heads. Each fiber-optic carrier terminates at an objective that allows focusing the laser on the target. Each objective is attached to a 6-axis precision mount (Thorlabs, K6X) with high-resolution rotational and translational motions, facilitating precise adjustments of the laser position and orientation. The kinematic mounts are attached on a single-axis linear stage (Newport 423, angular deviation $< 200 \mu\text{rad}$) to enable translating the lasers axially to selected positions along the rotational axis (the *axis average line*). The two lasers are arranged in a mutually-perpendicular orientation within a plane (i.e., the *plane of measurement*, which is perpendicular to the axis average line) by following the procedure described in [14]. The x and y measurement axes are set by the orientations of the two lasers. The vertical (y) laser is attached to a custom-made polymer granite arch, which is specially designed to provide a high level of damping and minimal vibrations. The horizontal (x) laser is attached to a polymer granite block. The spindle is housed in a cast iron holder, which is bolted onto another polymer granite block. Each of the polymer granite components are fixed to an optical table (Newport RS 4000 with tuned damping). A tube microscope ($1667\times$ magnification; $180 \times 135 \text{ mm}$ field of view) with a charge-coupled device (CCD, Sentech-07H6491) camera is placed on the optical table to assist in axial placement of the tools while clamping them on the spindle.

The LDV systems (Polytec OFV-552 with fiber-optic sensor head) are used with a displacement decoder (DD-500 analog displacement decoder), providing a frequency bandwidth of 350 kHz and a resolution of few picometers [23]. For accurate LDV measurements, the lasers are required to be perpendicular to and focused on the measurement surface. The procedure in [14] was used to align and focus the lasers on the measurement surfaces by adjusting the 6-axis mounts and the objectives, respectively. For this purpose, the strength of the reflecting laser light was monitored using a voltage indicator provided by the LDV system.

Although the approach presented in this work is applicable to any

microtool-collet-spindle assembly with an ultra-high-speed spindle, the experiments presented in this study were performed on an electrically driven, hybrid ceramic ball bearing miniature spindle (IBAG HT 45S140) with a maximum rotational speed of 140 krpm. The axial and radial static stiffness values at the spindle nose are specified by the manufacturer as $21 \text{ N}/\mu\text{m}$ and $24 \text{ N}/\mu\text{m}$, respectively [24]. The spindle is water cooled to maintain the internal temperature at $27^\circ \pm 2^\circ \text{C}$ through an external chiller unit. The spindle works with a MEGA4S collet system for clamping the tools (see Fig. 3(d)). The collet features a four-jaw design, and a collet nut is used to attach microtools onto the spindle. A collet wrench is used to tighten the collet nut to the recommended torque of 10 Nm.

For the radial throw measurements presented in this work, a commercial micro-endmill ($254 \mu\text{m}$ diameter tool with a 3.175 mm shank diameter) and a custom-fabricated microtool blank (1.5 mm diameter at tip with a 3.175 mm shank diameter) were used (see Fig. 3(e)). For each of the two samples, the form errors were estimated to be below $\pm 500 \text{ nm}$ from radial throw measurements at multiple locations at the shank portions. Since the overhang length of the tools affects the radial throw due to the tilt errors, the overhang length between different tests were kept within $5 \mu\text{m}$. For this purpose, the tube microscope was used to determine the edge position of the sample attached to the spindle, and subsequent adjustments to the attachment length were made until the overhang length is within $\pm 5 \mu\text{m}$ of the desired length of 15 mm . Before attaching each tool to the collet, and prior to taking each measurement, the tools were cleaned with pure ethyl alcohol using foam swabs.

The angular orientation of the spindle, θ , must be recorded simultaneously with the radial throw measurements. This is critical not only for correlating the radial throw with the rotation angle, but also for synchronizing separate measurements from multiple axial locations, as required for the determination of the tilt angle. For this purpose, an infrared (IR) sensor (Monarch Instrument, IRS-W) with a binary voltage output of 0 V or 5 V was used. The sensor outputs a 5 V signal when the infrared light is reflected from the surface to the sensor, and the signal sharply drops down to 0 V when a non-reflective surface, such as a small engraved mark, is encountered. On each tool shank, a $200 \mu\text{m}$ -wide reference mark parallel to the tool axis (see Fig. 3(c)) was created using laser engraving (LPKF ProtoLaser U3). For this mark width, a

sharp voltage drop occurs within two sampling points of the IR sensor, corresponding to a response time of 2×10^{-7} s. By tracking the voltage-drop location along the measured rotating surface, the start and end of each revolution can be detected with an angular resolution better than 0.08 deg for spindle speeds up to 130 krpm. The “reference” angle, θ_{IR} , measured by the IR sensor is directly related to the rotation angle θ , which is defined based on the reference (first) cutting edge of the tool. The relationship between these two angles are described in the following section.

Although the cooling system retains the coolant temperature within $\pm 2^\circ\text{C}$, this small temperature variations could still cause variations to radial motions of the spindle [11]. To assess the effect of spindle (coolant) temperature and the associated thermal cycles on radial throw measurement, a miniature resistance temperature detector (RTD, with $\pm 0.1^\circ\text{C}$ accuracy) is integrated into the coolant outlet line at 50 mm from the spindle outlet.

3.2. Data collection and post processing

Although the radial throw includes many frequency components, for the majority of UHS micromachining spindles, the radial motions are dominated by the one-per-rev components. As such, in this work, we focus on the one-per-rev (fundamental) component of the radial throw. In this section, we describe the post-processing of the measured data for obtaining one-per-rev radial throw magnitude and orientation at *any* location along the tool axis.

The radial throw variations due to thermal cycling were first assessed. For all the measurements presented in this work, the spindle was thermally stabilized by operating it for a 30 min warm-up period prior to any measurements. After the warm-up period, the thermal fluctuations and the associated changes in radial throw (at $z = 5$ mm) within a thermal cycle were obtained at two speeds. The temperature fluctuations follow a cyclic pattern with a period of 16 min for 60 krpm and 8 min for 120 krpm, respectively. Within each cycle, the fundamental component was seen to vary less than ± 42 nm at 60 krpm and ± 90 nm at 120 krpm, respectively. The variations in x and y directions were within 5 nm of each other. In reporting the results below, we provide the radial throw values obtained by averaging five measurements that are uniformly distributed within the entire thermal cycle for the selected spindle speed.

To determine the radial throw of the rotational axis at a given z position, the radial motions from the x and y directions at two separate axial positions (z_1 and z_2) of the tool shank must be measured while the tool is rotated at the selected speed. The angular orientation θ_{IR} is simultaneously obtained from the IR sensor measurements. A LabVIEW™ code was written to manage and synchronize the measurements.

The construction of radial throw from the measurements involves several post-processing steps before using the formulation described in the previous section. First, a 10 Hz non-causal high-pass filter was used to remove any LDV-related drift from the measured displacement data. Second, the IR sensor data was used to identify each rotation cycle (dashed lines in Fig. 4(a)) on the measured displacements. Third, the displacement from at least 500 cycles were superimposed to obtain the displacements in the angular domain, as seen in Fig. 4(b). Fourth, following the formulation in [5], the synchronous motion at a given rotation angle was calculated from the mean of the superimposed data at that angle. A sine function was then fitted to the synchronous motion in the least square sense to extract the amplitude (ρ_{ix} , ρ_{iy}) and phase (ϕ_{ix} , ϕ_{iy}), of the fundamental (one-per-rev) motions for each of the two measurement planes $i = 1, 2$ (see Fig. 4(b)). In this step, the angles (θ_{IR}) calculated from the IR sensor were transformed into rotational angle θ using the approach outlined below. The obtained amplitude and phase values were then substituted in the formulation to obtain the radial throw magnitude and orientation of an axis or of a cutting edge at any axial plane z .

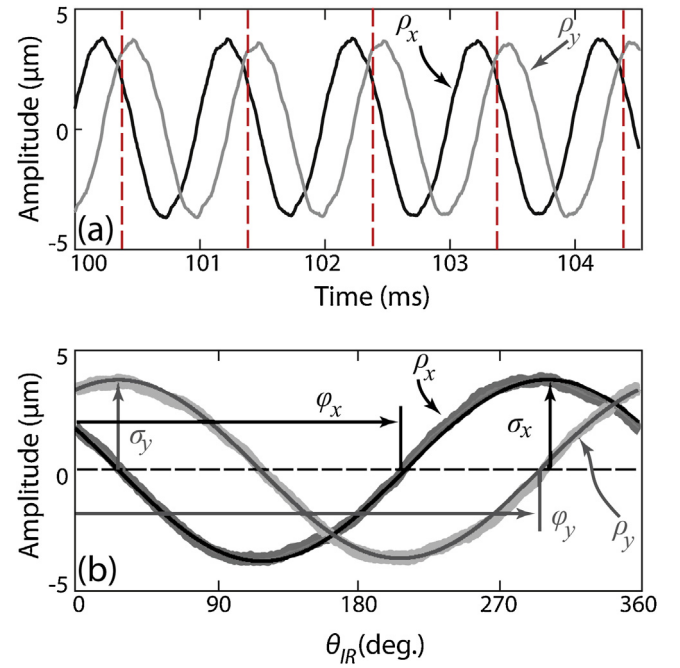


Fig. 4. The post-processing steps to obtain amplitude and phase of best fit sine: (a) raw displacement data along the x and y axes as ρ_x and ρ_y , respectively, (b) cycle-by-cycle averaged data, and the sinusoidal fit to obtain amplitude and phase of fundamental (one-per-rev) displacement components along x and y axes.

3.3. Determination of the rotation angle

The rotational angle, θ , is defined as the angular orientation of the reference cutting edge at the bottom of the tool—labeled as the *first* cutting edge—and is zero when the first cutting edge is passing through the positive x axis. Since θ cannot be directly obtained during the experiments, the angular orientation is measured with respect to the reference mark using the IR sensor data. In this section, we describe an approach for transforming the measured angular orientation θ_{IR} to the rotation angle θ .

Fig. 5 depicts a radial throw measurement. The IR sensor is located at an angle λ from the x axis, and the angle β identifies the orientation of the first cutting edge with respect to the reference mark. The rotation angle θ can be calculated as $\theta = \theta_{IR} + \lambda + \beta - 2\pi$. Thus, obtaining θ from θ_{IR} necessitates determining the angles β and λ .

The angle β indicates the relative orientation of the first cutting edge to the reference mark on the tool shank. As such, β is a property of the particular tool (with the reference mark) and is independent from the rotation angle. To find β for the micro tools used in our experimentation, a focus-variation microscope (Alicona G4 Infinite Focus) was used (see Fig. 6). The microscope is equipped with objectives up to $100\times$ magnification and with a high-precision rotation unit that provides roll and pitch motions. First, the microtool was attached on the rotation unit, and the alignment of the reference mark with respect to the edges of the tool shank was measured. Considering less than 500 nm of form error on both tools, this measurement indicated that the reference mark was aligned with the tool axis within 0.5 deg. Second, with the help of the microscope software, the orientation of the rotation unit was adjusted using micrometers to align the reference mark with the lateral direction of the field of view within 0.1 deg. This position was set as the reference position of the rotary stage. Third, the rotation unit was used to apply a 90 deg rotation about an axis perpendicular to a plane created by the reference mark and the tool axis. This makes the field of view to be normal to the tool axis, thus enabling viewing the bottom (cutting edges) of the tool. And fourth, the angle β was measured as the

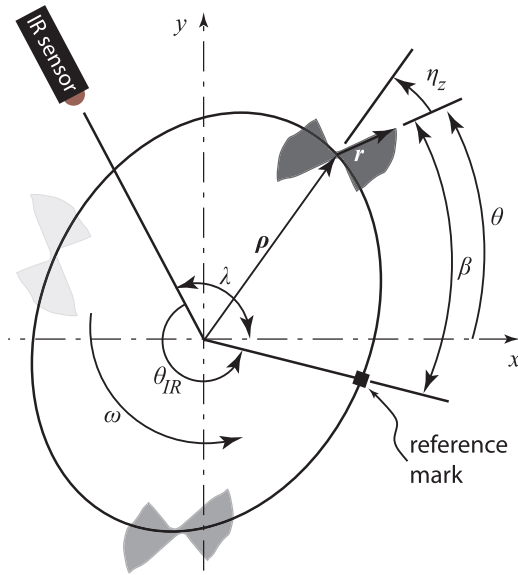


Fig. 5. The x-y plane at tool-tip to obtain orientation of radial throw with respect to the first cutting edge of the tool. For clarity, the cutting tool is drawn at a much smaller dimension than the magnitude of radial throw.

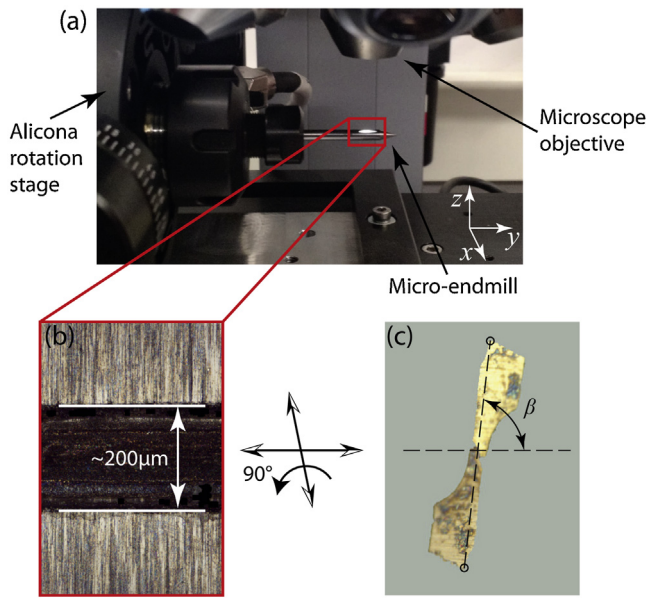


Fig. 6. Optical procedure to find the angle β between the reference mark and the cutting edge of a micro-endmill: (a) micro-endmill clamped to the rotary stage of the Alicona measurement system, (b) the reference mark on the tool shank, and (c) the tool-tip view after rotating the micro-endmill by 90 deg about the x-axis.

angle between the horizontal axis (where the reference mark was aligned) and the first cutting edge (see Fig. 6(c)). For each tool, the measurement was repeated five times, which indicated that the angle β is determined within ± 0.2 deg using this approach.

To determine the angle λ (the orientation of the IR sensor with respect to the x axis), the x-axis LDV and the IR sensor were simultaneously used to measure the orientation of the reference mark. For this purpose, the single axis linear stage was used to move the LDV along the tool axis until the laser spot was centered along the length of the reference mark. For this purpose, the reflectivity of the LDV is monitored to find the two lengthwise ends of the reference mark, and then the laser spot was moved to the center of the two ends using the precision stage. With this configuration, both the LDV (reflectivity signal) and the

IR sensor monitors the reference mark. The spindle was then operated at a relatively low speed (30 krpm), and the LDV-reflectivity and IR-sensor data were simultaneously recorded. In the angular domain, the LDV and IR reflectivity measurements were superimposed. The angle λ is identified as the angle between two subsequent signal drops. Measurements at low spindle speeds increase the resolution of angular measurements for a given sampling rate. At 30 krpm spindle speed, this approach enables determining λ within ± 0.3 deg.

4. Analysis of radial throw and experimental validation

The formulation presented above requires measurement of the radial throw at two axial positions along the shank region of a tool to predict the radial throw at the tip region of the tool. Thermal fluctuations, tool form errors, and uncertainties arising from environmental sources induce variations in radial throw measurements, thereby causing variations on the predictions. Furthermore, those variations could change with spindle speed. In this section, we first analyze the variations on radial throw at different spindle speeds. We then experimentally validate the radial throw predictions at different spindle speeds using a microtool blank. It is important to note that, due to the nature of the one-per-rev data, the radial throw follows a perfectly elliptical trajectory (including a circle being a special case of an ellipse).

4.1. Variations on radial throw predictions

Since we focus only on the one-per-rev component of the radial throw, the post-processing of the data eliminates any variation or uncertainty that does not contribute to the one-per-rev component [5]. In other words, any uncertainty/variation at asynchronous frequencies and at (super-) harmonics of the spindle frequency is removed by the data processing. However, uncertainties/variations at the spindle frequency will cause variations to the radial throw predictions. As described in [22], among different sources of environmental and measurement uncertainties, the largest contribution to the one-per-rev component of the radial throw arises from the vibrations between the laser objectives and the spindle base. Since the spindle is the main driver of those vibrations, they depend on the spindle speeds. As discussed in [11], although controlled in a closed-loop fashion within ± 2 degrees, the temperatures within the spindles follow a cyclic pattern about the set temperature, yielding relatively large variations on radial throw. In microtool shanks, form errors could be as large as (or larger than) ± 500 nm. When measured from a single axial location, the form errors contribute only to the harmonics of the rotational frequency: that is, they do not contribute to the one-per-rev component of the radial throw. However, when the radial throw is measured from two axial positions, the measurements yield a different rotational center (axis average line) for each axial position. As such, any non-straightness of the tool axis contributes variation to the calculated tilt, and thus, to the radial throw predictions.

In this work, we followed an experimental approach to evaluate the aforementioned uncertainties and variations on radial throw predictions. The experiments were conducted using a commercial micro-endmill with 254 μm diameter, and the tool was not removed from the spindle during the entire experimentation after being clamped on the collet. *First*, the thermal cycling of the spindle was determined by measuring the coolant temperature at the outlet of the spindle. *Second*, the radial throw was measured from five axial locations along the shank of a commercial micro-endmill at five specific temperatures that span the thermal cycle. These measurements were conducted at five spindle speeds (60k, 80k, 100k, 120k and 130k rpm). In each case, the radial throw data were collected for at least 600 revolutions. *Third*, the radial throw data was divided into sections of 20 revolutions, and the post-processing was performed to obtain the one-per-rev component for that data section. Thus, for each given set of axial location, temperature, and spindle speed, at least 30 one-per-rev components were obtained (one

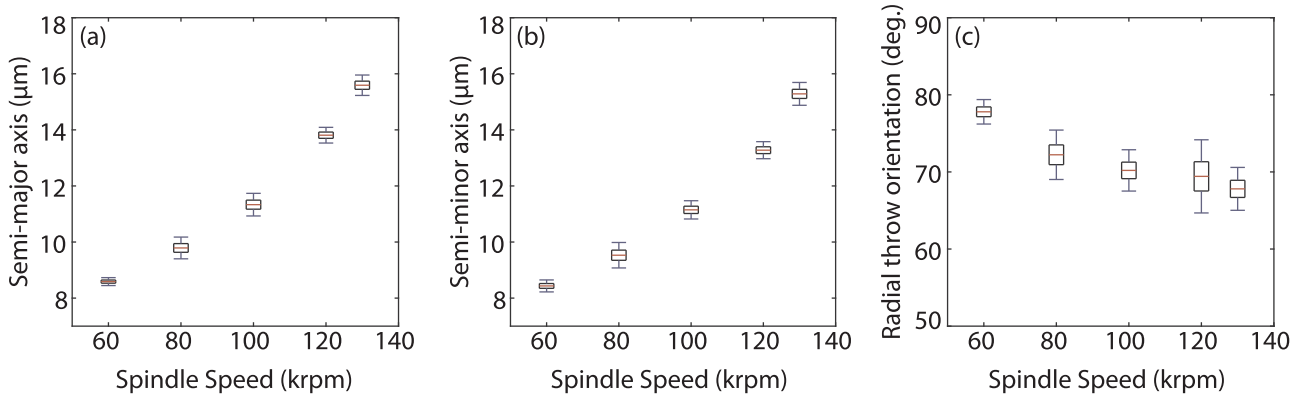


Fig. 7. Predicted radial throw at the tool-tip and the associated variations: (a) The semi-major and (b) the semi-minor axes, and (c) the radial throw orientation (η) as a function of spindle speeds.

per each of the 20-revolution data section). *Fourth*, for each given set of spindle speed and temperature, separate combinations of data were formed. Each combination includes data from two axial locations (out of five) and the radial throw from one of the data sections (out of more than 30). All combinations of the data were then used to predict the radial throw at 15 mm away from the spindle nose. *Fifth*, after compiling the data for each specific temperature, for a given spindle speed, all the radial throw predictions from the five temperatures were combined to determine the radial throw variations for that spindle speed.

Fig. 7 presents the predicted radial throw by providing the semi-major axis, semi-minor axis and radial throw orientation (at $\theta = 0$) at each of the tested spindle speeds. To represent the variations, a box-and-whisker plot is used. After removing the outliers using $\pm 2.5\bar{\sigma}$ approach [25], the median value is calculated, and the boxes are used to indicate the $\pm \bar{\sigma} = \pm 1.4826 \times \text{MAD}$, where MAD is the median absolute deviation [25]. In the case of normal distribution, $\bar{\sigma}$ is equal to the standard deviation. The whiskers are used to indicate the entire range after the outliers are removed.

As seen in Fig. 7(a) and (b), for this particular spindle-collet set, the difference between the semi-major and semi-minor axes is very small with respect to their average value. In other words, the trajectory closely resembles a circle. Since a circular trajectory has an arbitrary major axis, the orientation of major axes exhibits significant variations, spanning the entire 360 deg in some cases. As such, the orientation of the major axis is excluded from the present analysis. For other spindle/collet combinations, when the trajectory is distinctly elliptical, this parameter should be analyzed. The range of variations in semi-major and semi-minor axes is seen to be within ± 500 nm with $\bar{\sigma} = 200$ nm. As a percentage of the median values, this corresponds to a range of $\pm 5\%$ and a $\bar{\sigma}$ of 2%. The largest variation is observed for 80 krpm. The variations on radial throw orientation (at $\theta = 0$) were seen to reach ± 5 deg (at 120 krpm). Considering that these variations include those arising from thermal fluctuations, form errors, and environmental uncertainties, they are deemed reasonably small.

We will now assess the relative contribution from the three sources on radial throw variations. First, to assess the contribution only from the thermal cycling, data from only two axial locations (the first and the fifth) are used, thereby eliminating the variations due to the form error. By using only the median values of radial throw parameters for the entire 600+ revolutions, rather than considering the data-sections, the effect of environmental uncertainties are eliminated. The variations (one-sided) in semi-major axis, semi-minor axis and radial throw orientation due to the temperature cycling at each speed is presented in the form of bar chart in Fig. 8. A maximum variation of 85 nm in semi-minor diameter was observed at 130 krpm and a variation of less than one degree was observed in radial throw orientation across the tested speeds.

Next, the contribution of environmental effects as variations from

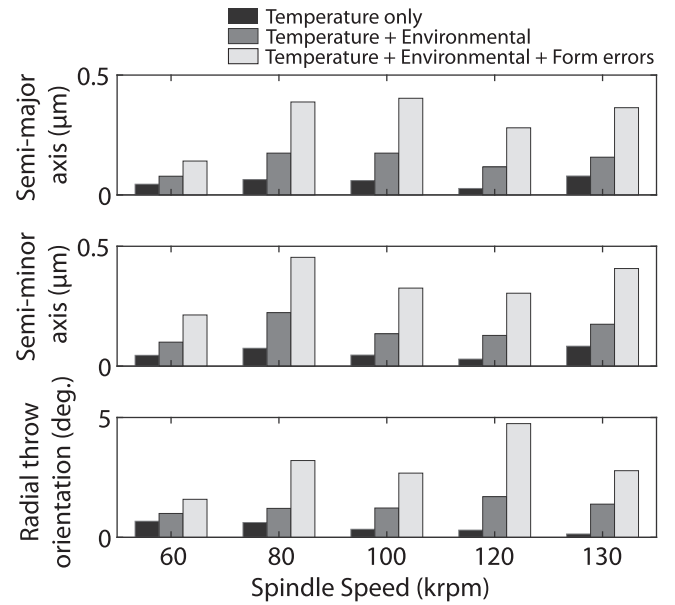


Fig. 8. One-sided variations ($2.5\bar{\sigma}$) due to various uncertainties (temperature, environmental and form errors) compounded one at a time for $z = 15$ mm.

data-section to data-section are added at each temperature step. Cumulative variations resulting from both the temperature and environmental effects are presented in Fig. 8. The variation in semi-major and semi-minor diameters increased by approximately 100 nm at most speeds when environmental effects are added. The variability in radial throw orientation increases by up to 1.5 deg.

Lastly, the effect of form errors is added to the thermal cycling and environmental effects. Addition of form errors increases the variations in semi-major and semi-minor diameters by approximately 200 nm at all speeds except 60 krpm (only 100 nm increase). Similarly, the variation in radial throw orientation is found to increase by up to 3 deg at 120 krpm. Based on the presented analysis, it is seen that the form errors are the major contributors to the variations in the prediction of radial throw at the tool-tip. This is expected because when two axial locations are sufficiently close to each other, small variations in the form results in a larger variation at the tip because of tilt-angle variations.

4.2. The effect of spindle speed on radial throw parameters and associated variations

Spindle speed directly affects the radial throw through the rotating eccentricity effect. This includes two components: the increase in radial

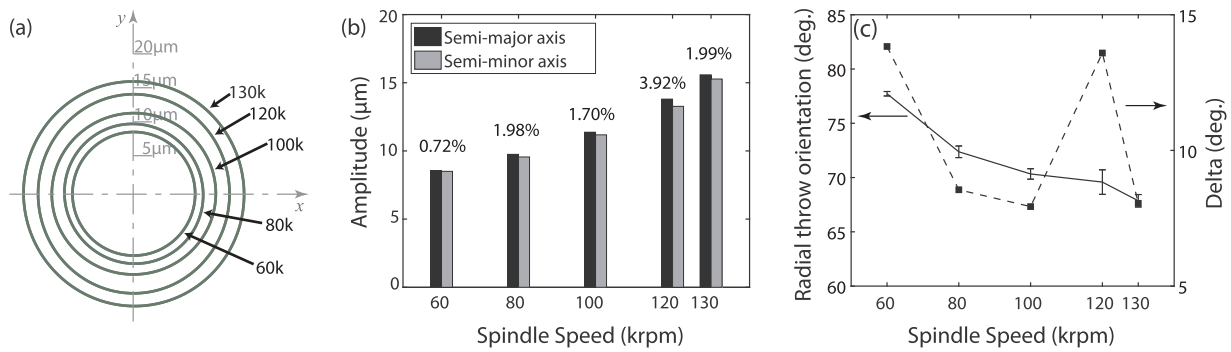


Fig. 9. The effect of spindle speed on radial throw: (a) polar plots in the x - y plane, where the center of the polar plot indicates the axis average line, (b) the percent difference between the semi-major and semi-minor axes (as a ratio of their average), and (c) trends in radial throw orientation η and angle between tool axis and eccentricity in x - y plane δ . The presented data corresponds to $z = 15$ mm.

force due to the rotating eccentricity and the change in effective stiffness due to the speed-dependent dynamic response of the spindle. As a result, the effect of spindle speed on radial throw could be significant.

The effect of spindle speed on radial throw magnitude is presented in Fig. 9(a) and (b). For this figure, the data measured from the microtool was used and the radial throw trajectories at 15 mm away from the spindle nose were predicted. Fig. 9(a) provides the polar plots of the radial throw, and Fig. 9(b) provides the median values of semi-major and semi-minor axes (and the percent difference between them as a ratio of their average) at different speeds. A significant increase in radial throw magnitude (both semi-major and semi-minor axes) is observed. Indeed, the radial throw magnitude almost doubles from 8 μm to 16 μm when speed is increased from 60 krpm to 130 krpm. The largest difference in semi-major and semi-minor axes is seen at 120 krpm at 3.92%: the trajectories at 60 krpm, 80 krpm, 100 krpm, and 130 krpm may be considered circular. The trajectory at 120 krpm is somewhat elliptical.

Fig. 9(c) shows the effect of spindle speed on the radial throw orientation (solid line). The radial throw orientation is seen to decrease with increasing spindle speed. The radial throw orientation is determined from both the magnitudes of the radial throw at two measurement planes, and the relative phase between the two radial throw trajectories. In other words, the orientation of the radial throw depends on not only the eccentricity and tilt, but also relative angle between the two. In our formulation, this relative angle is represented at the $z = z$ plane by angle δ (the dotted line in Fig. 9(c)). For the present case, δ was seen to vary between 7.93 deg and 13.83 deg across tested speeds, and the magnitude of eccentricity (not shown) increased from 3.65 μm at 60 krpm to 7.49 μm at 130 krpm. These combination of parameters resulted in a decrease in radial throw orientation by approximately 10 deg from 60 krpm to 130 krpm. The error bars in the orientation data are due to the variation in the radial throw orientation within a

rotation, and the amount of variation is correlated with the degree of ellipticity. For 120 krpm, the variation in radial throw orientation was seen to be within ± 2 deg within a rotation.

4.3. Experimental validation of radial throw predictions

A set of experiments is conducted to validate the presented approach by comparing the predicted radial throw to that directly measured from the tip portion. Since the flutes on a micro-endmill preclude measurements from the tip portion, a custom precision-ground carbide microtool blank with a cylindrical tip portion (3.125 mm shank- and 1.5 mm tip-diameter) was used for the validation experiments.

To account for the uncertainties and variations, the same experimental approach described above for the micro-endmill was performed here for the tool blank. The only difference is that the measurements were obtained from eight (instead of five) axial locations along the shank portion, since the longer length of the tool blank allowed measuring from more axial locations. The radial throw at the tool-tip (17.63 mm from the spindle nose) was measured for at least 600 revolutions, and the data was processed by using 20-revolution data sections to incorporate the variations in the measured radial throw. The formulation was used to predict the radial throw at the same location, along with the associated variations.

Fig. 10 shows the semi-major axis, semi-minor axes, and the orientation (at $\theta = 0$) of the measured (black dots) and the predicted radial throw at the tip, where the predictions indicate the entire data range after removing the outliers. Since there are no cutting edges to use as a reference for the radial throw orientation, we used the reference mark as the reference position in the calculations. The predictions include all the variations due to thermal fluctuations, form errors, and environmental uncertainties, including a median value, $\pm \sigma$ variations about the median (indicated with the box), and the entire data

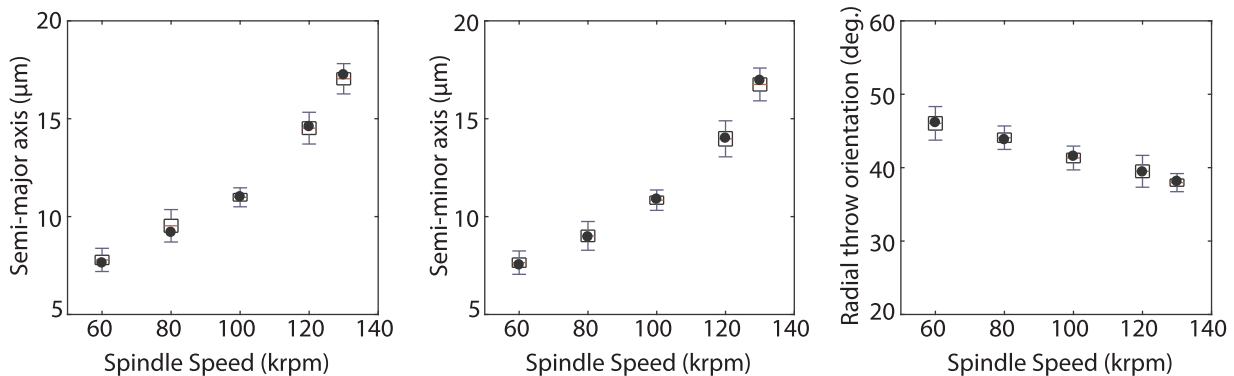


Fig. 10. Measured and predicted radial throw at the tip of a tool blank: (a) The semi-major, and (b) the semi-minor axes and radial throw orientation (η) are presented as a function of spindle speeds for tool-blank at 17.63 mm. The black dots represent the median of measured values.

range (indicated with whiskers) after removal of the outliers. The maximum variation (2.5σ) in measured data was found to be 150 nm for both semi-major and semi-minor axes, and 0.5 deg for radial throw orientation. Since the variation in measured data is reasonably small compared to the that of the predictions, only the median values are plotted in Fig. 10. It is noted that the predictions and measurements from the tool blank demonstrated the same trends (e.g., increased radial throw with increased speed) as those from the micro-endmill.

As seen in Fig. 10, all three radial throw parameters are predicted accurately, since the measured data falls within the median $\pm \sigma$ ranges. The largest errors between the median values of the prediction and the direct measurements were 3.5%, 1.5%, and 0.3 deg for the semi-major axis, semi-minor axis, and radial throw orientation, respectively. Based on these results, we conclude that the radial throw parameters are predicted accurately using the presented approach.

5. The effect of tool-attachment reproducibility on radial throw parameters

As outlined in the literature [11,18], the nature and precision of micro-tool/collet/spindle interfaces strongly affect the radial throw (and error) motions, and this effect is largest for the one-per-rev component. In this section, we present a statistical analysis on the changes of radial throw parameters due to repeated attachment/detachment cycles of the tool to the spindle. To isolate the variations arising only due to the attachment, the study was conducted at a single spindle speed (60 krpm), at a constant temperature within the thermal cycle (27 deg), from only two points along the shank of the micro-endmill, and without data-sectioning (that is, using the entire 600+ revolutions rather than 20-revolution sections). Since the radial throw trajectory closely resembles a circle at 60 krpm, the radial throw was only measured along the x direction, and the y direction radial throw was obtained by applying a 90 deg phase shift to the x data. The data was collected from 18 attachment/detachment cycles. For each subsequent attachment, the tool was completely taken out of the collet, cleaned with alcohol swabs and slid inside the collet after a random rotation about its axis. While tightening the collet nut, the tool was left untouched to prevent any bias that could be introduced by the operator. The overhang length of the tool was kept at $15 \text{ mm} \pm 5 \mu\text{m}$ using a high magnification tube microscope.

We analyzed five parameters: the eccentricity e ; the tilt angle ζ ; the angle δ between the tool axis and eccentricity in the x - y plane; the radial throw magnitude ρ_{15} ; and the orientation η_{15} at $z = 15 \text{ mm}$ from the spindle nose. Note that the radial throw parameters become independent of the rotation angle θ for a circular trajectory.

Fig. 11 provides the histograms for each of the five parameters. The Anderson-Darling normality test indicated that all parameters except the radial throw orientation follow a normal distribution with $p > 0.05$. The variations of the radial throw orientation were seen to span from 0 to 360 degrees. We discuss the nature and source of radial throw orientation variations in the following section. The standard deviations (as a ratio of the mean value) of eccentricity and tilt angle was seen to be 7.5% each. The standard deviation in δ was seen to be 3.13 deg. As a result, the predicted radial throw magnitude was seen to have a relative standard deviation of 6.9% with respect to its mean value of $8.17 \mu\text{m}$. As expected, the attachment/detachment cycles were found to have a significant effect on radial throw parameters. These variations could arise from the variability in the interactions between the tool/collet, collet/collet-nut, and collet-nut/rotor interfaces.

6. Contribution of spindle, collet and tool interfaces on radial throw orientation

The analysis presented in the previous section showed that the attachment/detachment cycles cause the radial throw orientation to vary considerably, spanning the entire range of 0 to 360 degrees. To better

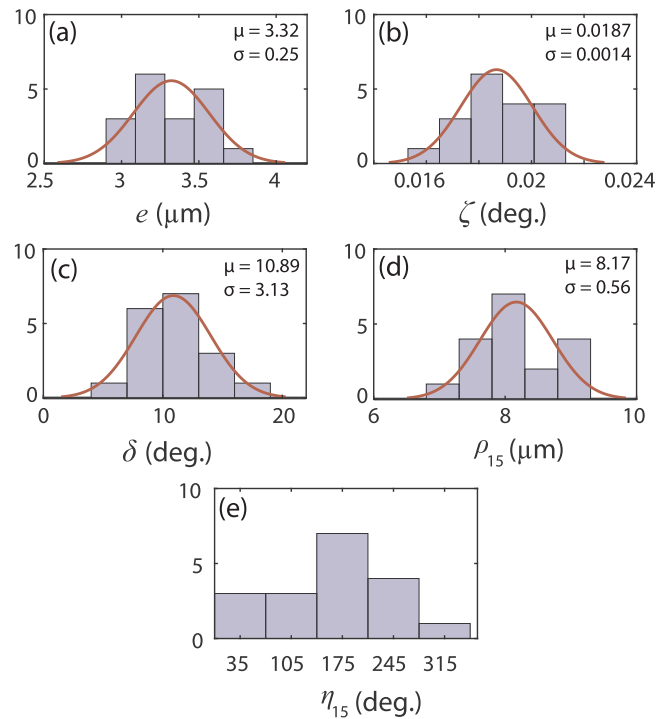


Fig. 11. Variation in the radial throw parameters due to repeated attachment/detachment cycles: (a) eccentricity e , (b) tilt angle ζ , (c) angle between tool axis and eccentricity in x - y plane δ , (d) magnitude of radial throw ρ , and (e) orientation of radial throw η , at $z = 15 \text{ mm}$. The red line indicates the normal distribution curve.

understand the nature and source of those variations, in this section, we present a study where the relative orientations between the spindle rotor (nose), collet, and microtool are specified, and the resulting changes in radial throw orientation are analyzed.

In reality, due to the limitations posed by the spindle and the collet, exact specification of the relative orientations is not feasible. For this reason, approximate orientations relative to the spindle rotor are provided to the collet and the tool, and then the actual orientations are obtained through direct measurements. The orientation of the spindle was obtained using a laser sensor pointed at the hexagonal nut that is permanently attached to and rotates with the spindle rotor. Due to the limitations of the laser sensor (Monarch Instruments, ROLS-W) and discontinuous data obtained from the nut's surface, this arrangement has a limited bandwidth of approximately 665 Hz. For this reason, all measurements in this study were performed at a rotational speed of 30,000 rpm (500 Hz). The relative orientation of the microtool with respect to the spindle was obtained by simultaneously measuring the angles of the nut (using the laser sensor) and the reference mark on the tool shank (using the LDV). To obtain the collet orientation, the axial surface of one of the four jaws of the collet was painted in black. High resolution images from a digital camera (oriented in the axial direction) were then obtained when the spindle was stationary, and the images were post-processed using MATLAB Image Processing Toolbox to determine the relative orientation between the collet and the spindle rotor. During the measurements, the tool overhang length was kept at $15 \text{ mm} \pm 5 \mu\text{m}$.

Fig. 12 illustrates the seven different targeted configurations. In each configuration, different orientations of the collet and the tool are specified with respect to that of the spindle. Table 1 gives the targeted and measured orientations of the collet and the tool relative to configuration I. In each configuration, the radial throw was measured from the shank at two positions, and the tool-tip radial throw orientations were predicted. Since our reference for the radial throw orientation is the “first” cutting edge of the tool, when the tool is reoriented by an

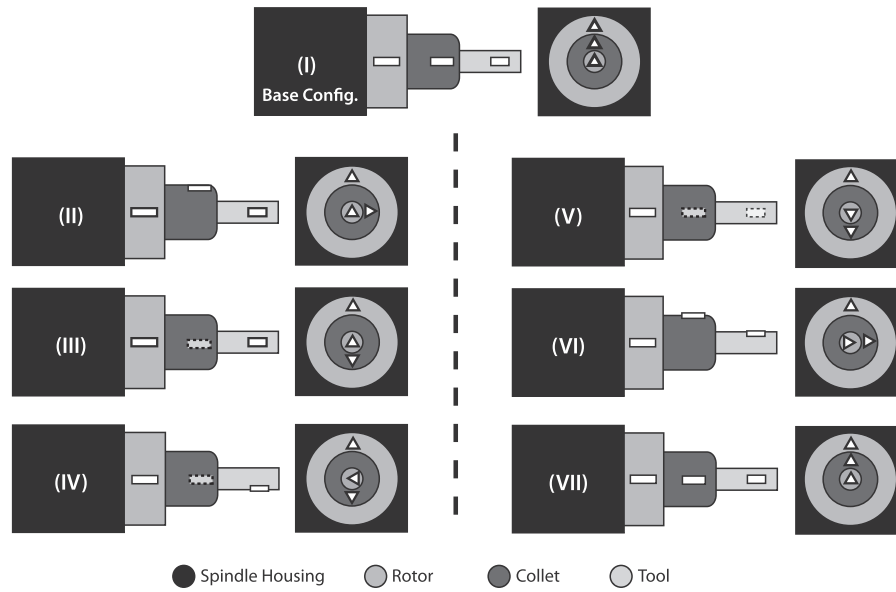


Fig. 12. Schematic representation of different tool-collet-spindle configurations. The white lines denote physical marks on each component.

Table 1

Targeted and measured angles provided to the collet and the tool, and the obtained radial throw orientations.

Config	Collet, η_c (deg)		Tool, η_t (deg)		Radial Throw Orientation (deg)	
	Targeted	Measured	Targeted	Measured	η	$\Delta\eta_t - \Delta\eta$
(I)	0	0	0	0.0	0.0	0
(II)	270	280.5	0	350.6	357.1	−6.4
(III)	180	192	0	331.2	343.8	−6.2
(IV)	180	195.6	90	61.4	68.3	5.7
(V)	180	196.6	180	150.8	155.8	2.0
(VI)	270	290.6	270	238.5	248.6	−5.1
(VII)	0	16.2	0	312.8	315.4	7.6

angle α , the radial throw orientation is expected to change directly by α since our measurement direction remains unchanged (see Fig. 5). From configuration I to II and from configuration II to III, the tool orientation with respect to the spindle was kept approximately constant, while the collet was rotated by approximately 90 degrees each time. Based on the last column of Table 1, these two 90-degree changes in collet orientation only brought 6.4 deg and 6.2 deg change to the radial throw orientation, respectively. From configuration III to IV and from configuration IV to V, the tool orientation was changed by 90 degrees each time while keeping the collet orientation constant (at approximately 180 deg). Similarly, these modifications only provided 5.7 deg and 2 deg change to the radial throw orientation, respectively. From configuration V to VI and from configuration VI to VII, the tool and the collet were rotated together by 90 degrees each time with respect to the spindle. The relative change in radial throw orientation was seen to be 5.1 and 7.6 degrees, respectively.

Based on these results, we conclude that the relative orientations between the tool, collet and the spindle induces only small changes to the radial throw orientation. That is, in the previous study when the spindle orientation was arbitrary, we observed that the radial throw orientation spanned the entire 360 degrees. However, when the spindle orientation is kept constant here, the change in radial throw orientation from the relative tool-collet-spindle orientations were less than 7.6 degrees. This indicates that the major contribution to the radial throw orientation arises from imperfections of the spindle itself. For instance, the non-straightness of the spindle rotor, or a misaligned spindle nose (the collet fitting) could cause such radial throw orientations. As such,

when the spindle orientation is kept constant between attachment/detachment cycles, significantly smaller variations to the radial throw orientation would be observed. Note that this conclusion is only valid for this particular spindle/collet combination.

Interestingly, this finding indicates that by specifying the orientation of the tool (i.e., the first cutting edge) with respect to that of the spindle, the radial throw orientation may be dictated within a broad range of angles (see the data from the previous section for radial throw magnitude). This may enable determining the most favorable radial throw orientation and setting that value during micromachining to reduce the surface location error, surface roughness, and/or chip thickness variations.

7. The effect of radial throw on surface roughness, dimensional errors, and chip-thickness variations

Radial throw critically affects the precision attainable from a milling process [26]. The changes in tool-tip trajectory arising from radial throw induces direct (kinematic) changes in sidewall surface roughness and dimensional errors (surface location error, SLE). In addition, radial throw alters the chip thickness experienced by each cutting edge, thereby causing changes in both machining kinematics and dynamics, and inducing an indirect change to quality parameters.

To assess the effects of the measured radial throw parameters on the roughness of the sidewall surface, deviations of channel width from the ideal width, and variations in chip thickness, we performed a simulation study. For this study, we considered only a single “slice” of a two-fluted microtool with 254 μm diameter. In addition to directly using the measured radial throw values presented above, considering the possibility of dictating the radial throw orientation as per the previous section, we included both the measured orientation and 45 degrees less than the measured orientation. For the simulations, Eq. (1) is used to generate the trochoidal trajectory of the cutting points. The SLE value is defined as half the average width of the channel, and the sidewall surface roughness is presented as Ra. To obtain the uncut chip thickness, an approach similar to that in [27] is adopted. The simulations were performed for feed rates of 5 μm and 25 $\mu\text{m}/\text{flute}$. The measured values of radial throw magnitude and orientation used in this section are presented in Fig. 7 above.

Fig. 13(a) presents the variation of SLE with spindle speed. As expected, following the increase in radial throw with increased spindle speed, the SLE also increases considerably with the spindle speed. An

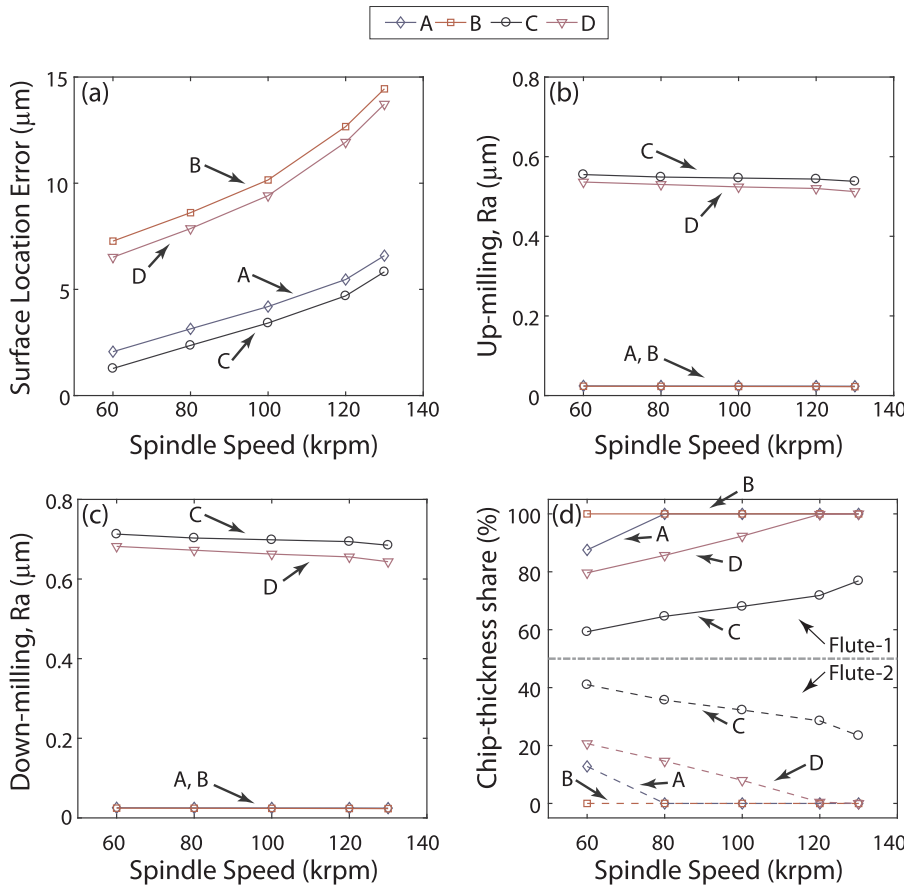


Fig. 13. The effect of measured radial throw on the (a) surface location error (SLE), (b) up-milling sidewall surface roughness, (c) down-milling sidewall surface roughness, and (d) chip-thickness share. η_m is the measured radial throw orientation. Case A: $5 \mu\text{m}/\text{flute}$ feed rate and $\eta = \eta_m$; Case B: $5 \mu\text{m}/\text{flute}$ feed rate and $\eta = \eta_m - 45^\circ$; Case C: $25 \mu\text{m}/\text{flute}$ feed rate and $\eta = \eta_m$; Case D: $25 \mu\text{m}/\text{flute}$ feed rate and $\eta = \eta_m - 45^\circ$.

increase in feed rate was seen to slightly reduce the SLE; however, this is merely due to the way in which the SLE is calculated. An increase in feed rate causes the cusp height to increase while not affecting the maximum channel width, and since the SLE is calculated as the average width of the channel, increased feed rate causes an apparent reduction in SLE. Another important observation is that the radial throw orientation has a significant effect on SLE. Indeed, a change in radial throw orientation by 45 degrees causes the radial throw to more than double for every speed. This also highlights the importance of being able to dictate the radial throw orientation. However, a deeper cut with non-zero helix angle tool will reduce the effect of radial throw orientation for the SLE of the entire channel, as the effect of radial throw at the cutting points will change at different depths.

The sidewall surface roughness (R_a) values for the up-milling and down-milling sides are given in Fig. 13(b) and (c). As expected, the surface roughness increases strongly with the feed rate, and increased spindle speed (and hence, increased radial throw magnitude) induces a slight decrease in sidewall surface roughness. The effect of radial throw orientation on sidewall surface roughness was seen to be less than 5%.

To assess the effect of radial throw parameters on uncut chip thickness, a *chip-thickness share* is defined as the ratio of maximum chip thickness (in the presence of radial throw) to twice the prescribed feed per tooth. As such, in the absence of radial throw, each of the two cutting edges have a chip thickness share of 50%. Fig. 13(d) shows the change in the chip-thickness share for each flute of a two-fluted micro-endmill for two spindle speed and two different feed rates. For Case A with $5 \mu\text{m}/\text{flute}$ feed rate (which is smaller than any measured radial throw magnitudes) and for the measured radial throw orientation, only one of the cutting edges participate in cutting for speeds above 60 krpm, i.e., 100% chip-thickness share. At 60 krpm, the measured radial throw orientation of 78° causes both cutting edges to engage into the material. For Case B, when the radial throw orientation is shifted from

Case A by 45 degrees, only a single cutting edge is involved in cutting for any speed. This is an expected result, since the measured radial throw magnitudes exceed the prescribed feed rate, and if the radial throw orientation is such that the radial throw is aligned with one of the cutting edges, only that cutting edge removes material. The smaller the feed rate and the larger the radial throw, the higher will be the non-symmetry in uncut chip thickness between the cutting edges. For Case C, with a feed rate of $25 \mu\text{m}/\text{flute}$ (which is larger than any measured radial throw magnitudes) and for the measured radial throw orientation, both cutting edges engage in cutting, although at different chip-thickness shares. The variation in chip-thickness share in this case is dominated by the change in radial throw orientation (see Fig. 9(c)). The closer is the radial throw orientation to 90 degrees (which was seen at lower speeds, e.g., 78° at 60 krpm), the more symmetric is the participation of the two cutting edges (i.e., the chip-thickness share is closer to 50%). In Case D, when the radial throw orientation is shifted (reduced) by 45 degrees, the small radial throw orientation angles at 120 krpm and 130 krpm causes only one of the cutting edges to participate in the cutting.

Radial throw will also cause changes in machining forces. The radial throw at the tool-tip changes the dictated tool-tip trajectory, thereby causing deviations in chip thickness from its “prescribed” value. This kinematic change in tool-tip trajectory can cause the machining forces to change significantly, both through the direct change in chip thickness, and through indirect change in specific energies due to the changing chip thickness. More indirectly, these variations in chip thickness may alter the process dynamics, thereby further affecting the machining forces.

8. Summary and conclusions

This paper presented a comprehensive approach for measurement

and analysis of radial throw in micromachining when using UHS spindles. First, a mathematical framework was constructed to obtain the trajectory of any point along the cutting edges in the presence of radial throw. The framework uses a vectorial formulation and requires measurements of radial throw at two axial locations along the tool shank in two mutually-perpendicular directions to determine the trajectory of the cutting points. An optical-microscope based approach was developed to relate the orientation of each cutting edge to the rotation angle of the spindle within ± 0.5 deg. Considering the major contribution to radial throw occurs at the spindle frequency, only the one-per-rev (fundamental) component of the radial throw was analyzed using the cycle-by-cycle averaging.

Subsequently, a statistical analysis on the variations of the radial throw measurements at different spindle speeds was presented. The form error of the tool shank was identified as the major contributor to the variations, followed by environmental vibrations and thermal fluctuations of the spindle. The maximum variation on the radial throw magnitude and orientation were below 2% (standard deviation) and ± 5 deg, respectively, with respect to their median values. The cutting edges were seen to follow a nearly circular trajectory, where the largest difference between the semi-major and semi-minor axes was 3.9% observed at 120 krpm. The radial throw magnitude was seen to increase significantly with spindle speed, from approximately $8\mu\text{m}$ at 60 krpm to approximately $16\mu\text{m}$ at 130 krpm.

The radial throw predictions at the tool-tip were then validated experimentally using a custom-fabricated microtool blank. The predictions were seen to fall within the $\pm \sigma$ ranges for any of the spindle speeds used during this work. The maximum difference between the mean values of the experimental and predicted radial throw magnitude and orientation were 3.5% and 0.3 deg, respectively.

Next, the changes in radial throw due to the repeated attachment/detachment of the microtool onto the spindle were analyzed. The radial throw parameters, with the exception of the radial throw orientation, were seen to follow a normal distribution. Multiple attachment/detachment cycles resulted in a 6.9% standard deviation on the radial throw magnitude at the tool-tip (at 15 mm from the spindle nose) at 60 krpm. To better understand the sources of variations on radial throw orientation, we studied the effect of relative configurations (orientations) of the tool, collet, and spindle. Relative configurations with more than 180 deg difference induced less than a 7.6 deg change to the radial throw orientation. The major contribution to the radial throw orientation was concluded to arise from the imperfections of the spindle. Thus, if the spindle orientation is kept constant, the repeated attachment and detachments contribute minimally to the changes in the radial throw orientation. As such, the radial throw orientation can be dictated to obtain the most favorable orientation that minimizes the effect of radial throw on the quality parameters.

A simulation-based study to examine the effects of the radial throw magnitude, orientation, and form on dimensional accuracy (channel width), surface roughness (on channel sidewalls), and flute-to-flute chip-thickness variations was then completed. As expected, SLE increases with increasing radial throw, and the radial throw orientation has a significant effect on SLE. The effect of radial throw on the R_a of the sidewall surface roughness was less than 5%. The chip thickness experienced by each cutting edge varied considerably with the radial throw magnitude and orientation.

Although we presented a comprehensive approach for measuring and analyzing radial throw in micromachining, including its effect on cutting edges on each flute, there are still a number of aspects that needs to be further explored. In our future work, we will (1) analyze the effects of tool overhang length on radial throw; (2) assess the tool-geometry inaccuracies and include their contribution in determining the radial throw at the tool-tip; and (3) develop a simplified

model—based on the spindle dynamics—to enable predicting the changes in radial throw with spindle speed.

Acknowledgements

The authors would like to acknowledge Drs. Alkan Donmez and Shawn Moylan from National Institute of Standards and Technologies (NIST) for discussing different aspects of the measurements and analysis. We also thank Bugra Ozutemiz for his assistance in engraving the reference marks on the micro-tools. This work is funded in part by the NIST award #70NANB12H208 (Ozdoganlar).

References

- [1] Dornfeld D, Min S, Takeuchi Y. Recent advances in mechanical micromachining. *CIRP Ann Manuf Technol* 2006;55(2):745–68.
- [2] Camara MA, Campos Rubio JC, Abrão AM, Davim JP. State of the art on micro-milling of materials, a review. *J Mater Sci Technol* 2012;28(8):673–85.
- [3] Bediz B, Korkmaz E, Khilwani R, Donahue C, Erdos G, Falo LD, Ozdoganlar OB. Dissolvable microneedle arrays for intradermal delivery of biologics: fabrication and application. *Pharm Res* 2014;31(1):117–35.
- [4] Yu JZ, Korkmaz E, Berg MI, LeDuc PR, Ozdoganlar OB. Biomimetic scaffolds with three-dimensional undulated microtopographies. *Biomaterials* 2017;128:109–20.
- [5] ISO 230-7 (2015): Test code for machine tools – Geometric accuracy of axes of rotation, 2015.
- [6] Lee K, Dornfeld DA. A study of surface roughness in the micro-end-milling process. Laboratory for Manufacturing and Sustainability; 2004.
- [7] Bediz B, Arda Gozen B, Korkmaz E, Burak Ozdoganlar O. Dynamics of ultra-high-speed (UHS) spindles used for micromachining. *Int J Mach Tools Manuf* 2014;87:27–38.
- [8] Lu X, Jamalain A, Graetz R. A new method for characterizing axis of rotation radial error motion: Part 2. Experimental results. *Precis Eng* 2011;35(1):95–107.
- [9] Lee CB, Zhao R, Jeon S. A simple optical system for miniature spindle runout monitoring. *Measurement: J Int Meas Confed* 2017;102:42–6.
- [10] Knapp B, Arneson D. Dynamic characterization of a micro-machining spindle. International conference on micromanufacturing (ICOMM), No. 108 2014.
- [11] Prashanth Anandan K, Burak Ozdoganlar O. Analysis of error motions of ultra-high-speed (UHS) micromachining spindles. *Int J Mach Tools Manuf* 2013;70:1–14.
- [12] Jun MB, DeVor RE, Kapoor SG. Investigation of the dynamics of microend milling—Part II: Model validation and interpretation. *J Manuf Sci Eng* 2006;128(4):901–12.
- [13] Nahata S, Prashanth Anandan K, Burak Ozdoganlar O. LDV-based spindle metrology for ultra-high-speed micromachining spindles. *Proc NAMRI/SME* 2013;41:319–24.
- [14] Prashanth Anandan K, Burak Ozdoganlar O. An LDV-based methodology for measuring axial and radial error motions when using miniature ultra-high-speed (UHS) micromachining spindles. *Precis Eng* 2013;37(1):172–86.
- [15] Grejda R, Marsh E, Vallance R. Techniques for calibrating spindles with nanometer error motion. *Precis Eng* 2005;29(1):113–23.
- [16] Smith PT, Vallance RR, Marsh ER. Correcting capacitive displacement measurements in metrology applications with cylindrical artifacts. *Precis Eng* 2005;29(3):324–35.
- [17] Hekman KA, Liang SY. In-process monitoring of end milling cutter runout. *Mechatronics* 1997;7(1):1–10.
- [18] Bao WY, Tansel IN. Modeling micro-end-milling operations. Part II: Tool run-out. *Int J Mach Tools Manuf* 2000;40(15):2175–92.
- [19] Malekian M, Park SS, Jun MBG. Modeling of dynamic micro-milling cutting forces. *Int J Mach Tools Manuf* 2009;49(7–8):586–98.
- [20] Nakkiew W, Lin CW, Tu JF. A new method to quantify radial error of a motorized end-milling cutter/spindle system at very high speed rotations. *Int J Mach Tools Manuf* 2006;46(7–8):877–89.
- [21] Liu X, Jun MBG, DeVor RE, Kapoor SG. Cutting mechanisms and their influence on dynamic forces, vibrations and stability in micro-endmilling. *ASME 2004 international mechanical engineering congress and exposition*. 2004. p. 583–92.
- [22] Prashanth Anandan K, Tulsian AS, Donmez A, Burak Ozdoganlar O. A technique for measuring radial error motions of ultra-high-speed miniature spindles used for micromachining. *Precis Eng* 2012;36(1):104–20.
- [23] Polytec OFV-5000 user manual.
- [24] IBAG. HT 45 S 140 user manual; 2011.
- [25] Leys C, Ley C, Klein O, Bernard P, Licata L. Detecting outliers: do not use standard deviation around the mean, use absolute deviation around the median. *J Exp Soc Psychol* 2013;49(4):764–6.
- [26] Schmitz TL, Couey J, Marsh E, Mauntler N, Hughes D. Runout effects in milling: surface finish, surface location error, and stability. *Int J Mach Tools Manuf* 2007;47(5):841–51.
- [27] Campomanes ML, Altintas Y. An improved time domain simulation for dynamic milling at small radial immersions. *J Manuf Sci Eng* 2003;125(3):416–22.